THE JOURNAL OF PHYSICAL CHEMISTRY B
A JOURNAL OF THE AMERICAN CHEMICAL SOCIETY

pubs.acs.org/JPCB

Article

Kinetic and Thermodynamic Control of G-Quadruplex Polymorphism by Na^+ and K^+ Cations

David A. Nicholson and David J. Nesbitt*

Cite This: *J. Phys. Chem. B* 2023, 127, 6842−6855

Read Online

ACCESS | Metrics & More | Article Recommendations

ABSTRACT: G-Quadruplexes (G4s) are ubiquitous nucleic acid folding motifs that exhibit structural diversity that is dependent on cationic conditions. In this work, we exploit temperature-controlled single-molecule fluorescence resonance energy transfer (smFRET) to elucidate the kinetic and thermodynamic mechanisms by which monovalent cations (K^+ and Na^+) impact folding topologies for a simple G-quadruplex sequence (5′-GGG-$(TAAGGG)_3$-3′) with a three-state folding equilibrium. Kinetic measurements indicate that Na^+ and K^+ influence G4 formation in two distinctly different ways: the presence of Na^+ modestly enhances an antiparallel G4 topology through an induced fit (IF) mechanism with a low affinity (K_d = 228 ± 26 mM), while K^+ drives G4 into a parallel/hybrid topology via a conformational selection (CS) mechanism with much higher affinity (K_d = 1.9 ± 0.2 mM). Additionally, temperature-dependent studies of folding rate constants and equilibrium ratios reveal distinctly different thermodynamic driving forces behind G4 binding to K^+ ($\Delta H^\circ_{bind} > 0$, $\Delta S^\circ_{bind} > 0$) versus Na^+ ($\Delta H^\circ_{bind} < 0$, $\Delta S^\circ_{bind} < 0$), which further illuminates the diversity of the possible pathways for monovalent facilitation of G-quadruplex folding.

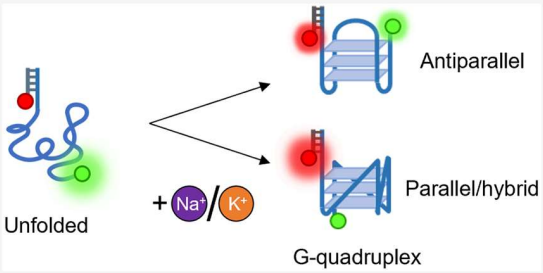

I. INTRODUCTION

G-Quadruplexes (G4s) represent ubiquitous nucleic acid secondary folding motifs that can form in G-rich DNA and RNA.[1] Stable under both *in vitro* and *in vivo* conditions, G4s play important roles in numerous biological contexts, including replication, transcription, and chromosomal stabilization.[2,3] Recently, G4s have drawn particular attention as potential drug targets for antiviral and anticancer therapies,[3−6] and G4 folds have been incorporated as modular components in DNA nanostructures.[7,8] A predictive understanding of the folding structure, kinetics, and thermodynamics of G4s in these diverse biological and biotechnological areas has proven to be elusive and requires a comprehensive knowledge of the underlying biophysics for nucleic acid folding.

In contrast with canonical nucleic acid duplex helical structures, G4s represent a highly structurally diverse secondary folding motif.[9,10] The signature element of the G4 structure is the presence of G-tetrads, planar arrangements of four noncanonically base-paired (and noncontiguous) guanine residues, which stack in layers ($n \approx 2$ or 3) to stabilize multiple G4 planes through adjacent $\pi-\pi$ interactions (Figure 1). The guanine residues in any single G4 plane can come from multiple nucleic acids as part of a higher-order molecular complex or from a single contiguous nucleic acid, in which case the G4 is termed a unimolecular fold. In such a unimolecular G4 fold, the four G-tracts (continuous G runs) in the G4 are spaced by short loop sequences (usually 2−3 nucleotides) to sterically allow the G-tracts to interact in a maximally hydrogen-bonded plane. The loops flexibly permit adjacent G-tracts to have the same or opposite 5′ to 3′ orientations, which allows G4s to fold into one of many topologies, each defined by a specific combination of the G-tract polarities.[11] G4 topologies are therefore classified as parallel (all strands sharing the same polarity), antiparallel (strands alternating polarities), or hybrid. Whether a G4 folds into a single topology or multiple, competing topologies (polymorphism)

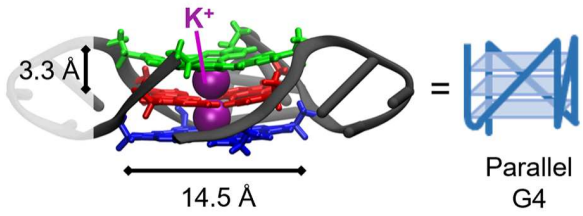

Figure 1. Crystal structure of a parallel G-quadruplex (G4). The three stacked G-tetrads are highlighted (green, red, and blue), and the two bound potassium ions are shown in purple (PDB 6IP3).

Received: February 14, 2023
Revised: June 17, 2023
Published: July 28, 2023

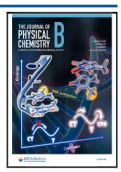

https://doi.org/10.1021/acs.jpcb.3c01001
J. Phys. Chem. B 2023, 127, 6842−6855

depends on many factors, including loop sequence.[12,13] G4 structural diversity is further increased by the presence of partially folded intermediates such as G-triplexes (G3) or G-duplexes (G2), which can also be populated significantly and readily interconvert with fully folded G-quadruplexes.[14,15]

G4 folding is accompanied by obligate binding of cations to the central channel formed by the stacked G-tetrads.[16] While this binding site is capable of binding polyvalent cations, it greatly favors monovalent cations, especially potassium (K^+). Importantly, the structure adopted by a G4 is regulated by the identity of its bound cation(s), which has been a subject of much research activity.[16−18] For example, the human telomere G4 sequence tends to fold into a parallel or hybrid topology in K^+ solution and an antiparallel topology in Na^+ solution.[19,20] The influence of ions on G4 folding has been studied extensively by bulk methods;[10,12,13,21−28] however, the polymorphism of G4s can make such ensemble results difficult to interpret. Conversely, single-molecule experiments are more ideally suited to resolve topology-specific properties in multistate folding systems.[29] In particular, single-molecule methods have been used to examine many aspects of G4 folding,[30] including G4 folding kinetics[31−35] and the temperature dependence of the folding equilibrium constants.[36] However, temperature-dependent studies of the folding kinetics at the single-molecule level have yet to be reported, which in principle would provide the first access to the thermodynamics of the transition states for G4 formation.

As a focus of the present work, we use temperature-dependent single-molecule microscopy to investigate the influence of monovalent cations (K^+ and Na^+) on the kinetics and thermodynamics of G4 folding. Specifically, we study the folding of the 5′-GGG-$(TAAGGG)_3$-3′ sequence, which is known to form a polymorphic G4.[34] We examine this system using fluorescence resonance energy transfer (FRET) to monitor the dynamics of G4 folding with a single-molecule FRET (smFRET) total internal reflection fluorescence (TIRF) microscope.[37] Transitions between the polymorphic network of G4 states are observed in real time, from which we determine the equilibrium constants and rate constants for these transitions. By analyzing the dependence of such folding dynamics on cation concentration and temperature, we obtain the first quantitative insights into the kinetic mechanism for polymorphism control by K^+ and Na^+ as well as the thermodynamics of cation binding to G4.

II. METHODS

G-Quadruplex FRET Construct. The single-molecule construct used in these studies consists of two annealed DNA oligomers. The first oligomer is a Cy3-labeled DNA G-quadruplex fold (5′-GGG-$(TAAGGG)_3$-3′) connected by eight thymine residues to an 18-nucleobase duplex-forming domain (full sequence: 5′-TGGCGACGGCAGCGAGGC-T_8-GGG-$(TAAGGG)_3$-Cy3-3′). For control experiments, a non-folding sequence was also utilized as the first oligomer (5′-TGGCGACGGCAGCGAGGC-T_8-GGTGAGTGGGAGT-GGTGTGTA-Cy3-3′). The second oligomer is complementary to the duplex-forming domain and is labeled with Cy5 and biotin (5′-Cy5-GCCTCGCTGCCGTCGCCA-Biotin-3′) for surface tethering by biotin−streptavidin interactions.[38] Both oligomers are purchased in HPLC-purified form from Integrated DNA Technologies and used as is. (Company names listed herein are in the interest of completeness and do not reflect endorsement of a particular vendor.) The oligomers are annealed by mixing 10 μM aliquots (1 M = 1 mol/L) and heating to 85 °C in order to disrupt intramolecular base-pairing before slowly cooling to room temperature at 1 °C/min. The annealed construct is used without purification, as constructs lacking the biotinylated strand do not adhere to the surface and constructs lacking the Cy3-labeled strand are inefficiently excited by the laser ($\varepsilon_{Cy5}/\varepsilon_{Cy3}$, the ratio of Cy5 and Cy3 molar absorption coefficients, is 3% at 532 nm).

Sample Preparation and Single-Molecule Microscopy. Sample preparation and single-molecule microscopy are carried out according to previously described protocols.[39,40] In brief, a glass coverslip is cleaned by soaking for 24 h in acetone, followed by a 30 min treatment with UV-generated ozone. The coverslip surface is incorporated into a flow cell, where it is functionalized by sequential 10 min exposure to buffered solutions of (i) 10 mg/mL bovine serum albumin (BSA) with 1 mg/mL biotinylated BSA, (ii) 0.2 mg/mL streptavidin, and (iii) 150 pM smFRET construct. This process produces a surface decorated with approximately 1 smFRET construct per 10 μm^2. The surface-tethered constructs are then imaged in 50 mM HEPES buffer (pH 7.6) with an oxygen scavenging cocktail to extend the observation time (100 nM protocatechuate 3,4-dioxygenase; 5 mM protocatechuic acid) and 2 mM Trolox to increase fluorophore brightness by quenching fluorophore triplets to the ground state.[41,42] Sodium and potassium levels are controlled by titration with NaCl and KCl solutions, respectively.

The prepared sample is observed with a through-objective TIRF microscope,[43] which permits 532 nm excitation of Cy3 molecules constrained to within ≈ 100 nm of the surface. The fluorescence from the smFRET construct is collected and separated by dichroic mirrors into Cy3 and Cy5 channels before being directed onto an intensified charge-coupled device (CCD) camera operating at 10 frames per second. Movies are analyzed by software written in LabWindows/CVI, which identifies particle locations by thresholding and extracts raw donor and acceptor fluorescence trajectories by integration over the local 4 × 4 pixel neighborhood for each frame. Background fluorescence levels are determined by fits of particle point spread functions to a symmetric 2D Gaussian function (equal full width at half-maximum (fwhm) for x and y), which permits calculation of background-corrected donor ($D(t)$) and acceptor ($A(t)$) signals. Time-dependent FRET trajectories are determined from the energy transfer efficiency, $E_{FRET}(t) = A(t)/(A(t) + \gamma D(t))$, where γ is the ratio of acceptor to donor detection efficiencies, which is determined to be nearly unity ($\gamma = 0.97$) via intensity changes during acceptor photobleaching.[44] Temperature control is achieved through a thermoelectric element that is in thermal contact with the sample and capable of servoloop heating and cooling to within 0.1 °C stability, as has been previously described.[40]

Hidden Markov Modeling. Rate constants for conformational transitions are determined by hidden Markov modeling analysis of the FRET trajectories.[45] The model consists of n states, each with a Gaussian-distributed FRET observable, $P(E_i, \sigma_i) \propto \exp[-(E - E_i)/2\sigma_i^2]$, where E_i and σ_i represent the FRET center and width of state i, respectively. Transitions between states occur according to first-order kinetics, as contained in the rate matrix $\mathbf{K}$, where K_{ij} is the unimolecular rate constant for the transition from state j to state i, and $K_{ii} = -\Sigma_{j\neq i} K_{ij}$. The transition probability per frame is then calculated via the matrix exponential $\mathbf{T} = \exp(\mathbf{K}t_{frame})$, where t_{frame} is the experimental time (0.1 s) between consecutive

https://doi.org/10.1021/acs.jpcb.3c01001
J. Phys. Chem. B 2023, 127, 6842−6855

frames. The likelihood function for a single trajectory is therefore described by the matrix product

$$L = \mathbf{1}^T \left[\prod_{i \geq 2} \mathbf{O}(E_i)\mathbf{T} \right] \mathbf{O}(E_1)\mathbf{p}_{eq} \tag{1}$$

where $\mathbf{p}_{eq}$ is the equilibrium probability vector ($\mathbf{K}\mathbf{p}_{eq} = 0$), E_i is the ith observed FRET value, $\mathbf{O}(E)$ is an $n \times n$ diagonal matrix with diagonal entries $O_{ii}(E)$ equal to the probability density of observing the FRET value E in the ith state, $\mathbf{1}^T$ is the row vector $(1, 1, \cdots)$ of length equal to the number of states n, and the product is taken over all frames in the trajectory except the first. For multiple trajectories, the total likelihood function is the product of the single-trajectory likelihood functions ($L_{total} = \prod_i L_i$). The maximum likelihood estimate of K_{ij}, E_i, and σ_i is obtained by performing a gradient ascent on L_{total} using MATLAB, with bootstrapping analysis performed to estimate uncertainties.[46] Each kinetic analysis includes 100−150 molecules and 2000−3000 observed transitions between FRET states.

Three-State Hill Fit. Population versus concentration data for the G4 are fit to a Hill model. The standard Hill equation describes ligand binding in systems with two distinguishable receptor configurations: a ligand-bound state and a ligand-free state.[47] However, the G4 construct in this work has three observable states, so we instead used a modified Hill analysis in order to include all three states. The binding model consists of two competing ligand association processes, which convert a receptor R into one of two distinguishable ligand-bound species B_1 or B_2, each potentially with its own stoichiometry (n_1 and n_2) and dissociation constants ($K_{d,1}$ and $K_{d,2}$):

1:

$$R \xrightarrow{+n_1 L} B_1 \qquad (K_{d,1})^{n_1} = \frac{[R]}{[B_1]}[L]^{n_1} \tag{2}$$

2:

$$R \xrightarrow{+n_2 L} B_2 \qquad (K_{d,2})^{n_2} = \frac{[R]}{[B_2]}[L]^{n_2} \tag{3}$$

The above dissociation constant expressions can be readily manipulated to yield the fractional populations in each state as a function of ligand concentration:

$$\theta_R([L]) = \frac{[R]}{[R] + [B_1] + [B_2]} = \frac{1}{1 + \left(\frac{[L]}{K_{d,1}}\right)^{n_1} + \left(\frac{[L]}{K_{d,2}}\right)^{n_2}} \tag{4}$$

$$\theta_{B_1}([L]) = \frac{[B_1]}{[R] + [B_1] + [B_2]} = \frac{\left(\frac{[L]}{K_{d,1}}\right)^{n_1}}{1 + \left(\frac{[L]}{K_{d,1}}\right)^{n_1} + \left(\frac{[L]}{K_{d,2}}\right)^{n_2}} \tag{5}$$

$$\theta_{B_2}([L]) = \frac{[B_2]}{[R] + [B_1] + [B_2]} = \frac{\left(\frac{[L]}{K_{d,2}}\right)^{n_2}}{1 + \left(\frac{[L]}{K_{d,1}}\right)^{n_1} + \left(\frac{[L]}{K_{d,2}}\right)^{n_2}} \tag{6}$$

This model is then applied to data for sodium and potassium titrations of the G-quadruplex, where $L = Na^+$ or K^+, R is the low FRET state, B_1 is the middle FRET state, and B_2 is the high FRET state. Dissociation constants ($K_{d,i}$) and apparent stoichiometries (n_i) are determined by simultaneously fitting all three populations to the Hill model using the weighted, nonlinear least-squares regression tools available in OriginPro.

van't Hoff and Arrhenius Analyses. Temperature-dependent equilibrium constants determined from hidden Markov modeling are then subjected to van't Hoff analysis,[48,49] wherein the Gibbs free energy

$$\Delta G^\circ = \Delta H^\circ - T\Delta S^\circ = -RT \ln(K_{eq}) \tag{7}$$

is rewritten in van't Hoff form

$$\ln(K_{eq}) = \frac{-\Delta H^\circ}{R}\left(\frac{1}{T}\right) + \frac{\Delta S^\circ}{R} \tag{8}$$

and where K_{eq} is the equilibrium constant, R is the gas constant (8.314 J/mol K), T is the absolute temperature, ΔH° is the reaction enthalpy, and ΔS° is the reaction entropy. In accord with such a van't Hoff model, we assume ΔH° and ΔS° to be approximately constant over the explored temperature range and perform a linear least-squares fit of $\ln(K_{eq})$ versus $1/T$ to extract ΔH° and ΔS° via the slope and intercept, respectively. In analogous fashion, the temperature-dependent rate constants can be analyzed in the context of Kramers' theory[50−52] to yield an Arrhenius-type expression

$$\ln(k/\nu) = \frac{-\Delta H^\ddagger}{R}\left(\frac{1}{T}\right) + \frac{\Delta S^\ddagger}{R} \tag{9}$$

where k is the rate constant, ν is the attempt frequency along the reaction coordinate, and $\Delta H^\ddagger$ and $\Delta S^\ddagger$ are the activation enthalpy and entropy, respectively. The attempt frequency is estimated as 1×10^6 s^{-1} from previous RNA folding studies,[50,51] but its actual value is dependent on the structure of the free energy landscape. As a consequence, the activation entropy $\Delta S^\ddagger$ is only weakly (i.e., logarithmically) sensitive to ν and not determined absolutely; however, any differential change in this entropy ($\Delta\Delta S^\ddagger$), for instance, due to change in ionic conditions, remains rigorously independent of the choice of ν.

III. RESULTS

The G-Quadruplex smFRET Construct Exhibits Multi-state Folding. To probe the thermodynamics of G-quadruplex folding at the single-molecule level, we designed a fluorophore-labeled DNA construct for FRET microscopy (Figure 2A). The folding domain of the construct consists of a repeated six-nucleotide sequence (5′-TAAGGG-3′), which forms a G-quadruplex with three stacked G-tetrads. This sequence is closely related to the human telomeric G4 sequence (5′-TTAGGG-3′), differing only by a single nucleotide mutation in the loop (TAA versus TTA), which has been previously observed by Tippana et al. to increase polymorphism.[34] The construct is labeled with the Cy3-Cy5 FRET pair[42] such that folding of the G-quadruplex brings Cy3 and Cy5 in closer proximity, increasing the energy transfer efficiency (E_{FRET}) between the fluorophores. The full construct is surface-tethered by biotin−streptavidin interactions[38] in order to enable the observation of the G-quadruplex in a single-molecule fluorescence microscope.

Temporal trajectories in a 100 mM Na^+ buffer reveal multiple, distinct E_{FRET} states which interconvert/equilibrate on time scales of 100 ms to seconds (Figure 2B). A histogram of E_{FRET} values gathered from $N = 83$ molecules is well-fit as a

https://doi.org/10.1021/acs.jpcb.3c01001
J. Phys. Chem. B 2023, 127, 6842−6855

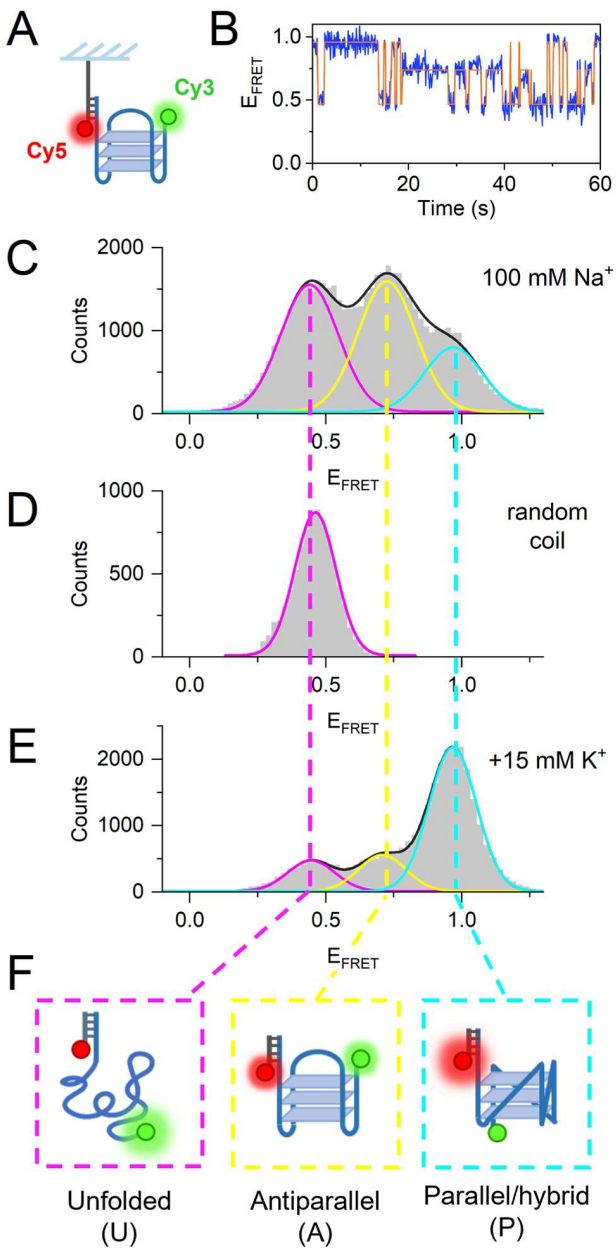

Figure 2. (A) The G-quadruplex smFRET construct design that is labeled with Cy3 and Cy5 for FRET detection of the conformational dynamics. (B) A sample smFRET trajectory taken in a 100 mM Na^+ buffer. The fitted state trajectory from hidden Markov modeling with the three states is overlaid in orange. (C) A FRET histogram (gray) aggregated from N = 83 trajectories. Gaussian fits (solid lines) are used to determine the FRET efficiencies and the relative abundance of the three states. (F) Cartoons that indicate putative structures of the three states: the unfolded state (E_{FRET} = 0.45), the antiparallel G4 state (E_{FRET} = 0.73), and the parallel or hybrid G4 state (E_{FRET} = 0.97). See text for details.

sum of three Gaussian distributions (E_{low} = 0.45, E_{middle} = 0.70, and E_{high} = 0.94), which corresponds to three construct conformations with resolved interfluorophore distances (Figure 2C). Three distinct FRET states were also observed in the work of Tippana et al. on this sequence.[34] To probe the identity of the FRET states, we first measured the FRET efficiency of a construct with a similar nucleotide composition but reordered it so that it cannot fold into a G4 or other secondary structures (Figure 2D). The FRET efficiency of this ssDNA construct (E_{ssDNA} = 0.46) is in good agreement with that of the low FRET state (E_{low} = 0.45). Therefore, we assign the E_{low} state as an unfolded G4 (U) in a single-stranded random coil configuration. The two higher FRET states are likely two different G4 topologies. To identify these states, we next introduce K^+ to the imaging solution, as K^+ is known to stabilize parallel or hybrid G4s and decrease the population of antiparallel configurations.[10,16−18] In 15 mM K^+, the FRET distribution shifts to favor the E_{high} state (Figure 2E) and reduces the population of the E_{low} and E_{middle} states. As a result, we assign the E_{high} state as either a parallel G4 or a hybrid G4 (P) and the E_{middle} state as an antiparallel G4 (A). All three putative structures (U, A, and P) are shown in Figure 2F.

Sodium Ions Indiscriminately Drive the Folding Equilibrium to the Antiparallel and Parallel/Hybrid Topologies. We first explored G-quadruplex folding as a function of Na^+ concentration at ambient temperature (23 °C). The FRET histograms in Figure 3A reveal an overall shift from the unfolded state (U) to the antiparallel (A) and parallel/hybrid (P) G4 topologies with increasing [Na^+]. Integration over these histogram peaks yields the subpopulation fractions in [Na^+] = 50−300 mM (Figure 3B), which can then be fit globally to a three-state Hill model (eqs 4−6) that explicitly includes all three interconversion routes. The least-squares fits to such a multistate model are shown as solid lines in Figure 3B, yielding the stoichiometric coefficient (Δn) for Na^+ binding and dissociation constants (K_d) for each interconversion pathway, as summarized in Table 1 (note that the cation binding stoichiometry reflects the *change* in the number of bound ions during folding, where it is possible that the unfolded state is already bound to one or more ions prior to folding). Interestingly, the unfolded state gains only one Na^+ ion when folding into either G4 state ($\Delta n_{U\to A} \approx \Delta n_{U\to P} \approx 0.87 \pm 0.09$), though Na^+ has a two-fold stronger affinity for antiparallel G4 (K_d = 132 ± 9 mM) than for parallel/hybrid G4 (K_d = 228 ± 26 mM). Conversely, there is no difference within the experimental uncertainty in the number of Na^+ ions bound to the two G4 conformations. As a consequence of the A and P states both binding one Na^+ ion, the A → P equilibrium saturates to a fixed ratio at high [Na^+] (Figure 3B). Na^+ clearly promotes G4 polymorphism, with the G4 construct populating both the antiparallel and parallel/hybrid topologies, even at [Na^+] = 300 mM.

Additional mechanistic insight can be obtained from the kinetic analysis of the Na^+ dependence of G-quadruplex folding events in the time domain. Rate constants for folding are determined by hidden Markov modeling (HMM) of smFRET trajectories[45,53,54] using a three-state model which includes all six rate constants describing forward and reverse interconversion between each FRET pair (Figure 4A), with the rate constants for G4 folding as a function of [Na^+] = 50−300 mM summarized in Figure 4B. As a rigorous thermodynamic check on the validity of these extracted rate constants, we can calculate the free energy sum around the three-state cycle (ΔG_{cycle}) at each Na^+ concentration and plot the values in Figure 4C:

$$\Delta G_{cycle} = -k_B T \ln\left(\frac{k_{U\to A}k_{A\to P}k_{P\to U}}{k_{A\to U}k_{P\to A}k_{U\to P}}\right) \quad (10)$$

By detailed balance, the free energy sum around any cycle of states must equal zero. Indeed, the calculated $\Delta G_{cycle}/k_B T$

https://doi.org/10.1021/acs.jpcb.3c01001
J. Phys. Chem. B 2023, 127, 6842−6855

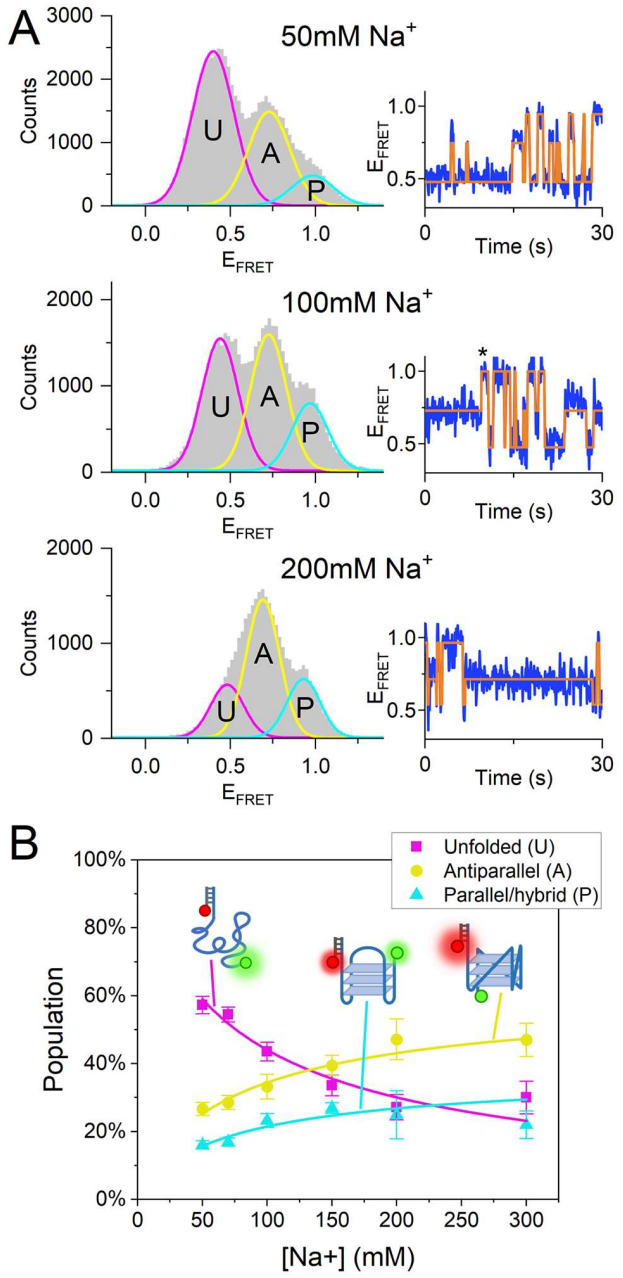

Figure 3. Influence of Na^+ on G4 folding equilibrium. (A) FRET histograms and sample FRET trajectories at 50, 100, and 200 mM Na^+. An example of a direct A → P transition is indicated by an asterisk. (B) The population of the three G4 conformational states in $[Na^+]$ = 50−300 mM. Fits to a three-state Hill model are shown as solid curves.

values vanish within uncertainty ($\pm 0.2\ k_BT$) for all Na^+ concentrations. In Figure 4B, the rate constants for the conversion of U to and from the G4 conformations A and P have the largest magnitude, while transitions directly between the antiparallel (A) and parallel/hybrid (P) G4 topologies are a minor, though not entirely forbidden, kinetic process (Figure 3A).

To additionally explore the effects of the Na^+ cation on G-quadruplex folding, we have further developed an explicit six-state kinetic model for Na^+ binding to the G-quadruplex (Figure 4D). The model consists of three DNA conformations,

Table 1. Results of Fitting G-Quadruplex Population Data vs $[Na^+]$ and $[K^+]$ to the Three-State Hill Model[a]

Transition	Parameter	Na^+	K^+
U → A	Δn	0.87 ± 0.09	−0.05 ± 0.05
	K_d (mM)	132 ± 9	–
U → P	Δn	0.87 ± 0.09	0.62 ± 0.05
	K_d (mM)	228 ± 26	1.9 ± 0.2
A → P	Δn	0.00 ± 0.09	0.67 ± 0.07
	K_d (mM)	–	2.9 ± 0.3

[a]U is the unfolded state (low E_{FRET}), A is the antiparallel G4 state (intermediate E_{FRET}), and P is the parallel/hybrid G4 state (high E_{FRET}). Uncertainties are reported as standard errors of the mean. For processes with Hill coefficients (Δn) equal to zero within uncertainty, dissociation constants (K_d) are not reported.

each with ligand-free and ligand-bound forms, which topologically generate a triangular prism (hence the "Tobler-one" model moniker). In accordance with the 1:1 Na^+ binding stoichiometry from the Hill fit of the population data (Table 1), the kinetic model includes a single Na^+ ion in each ligand-bound state. Ligand binding kinetics are modeled to be much faster than subsequent G4 conformational dynamics,[16,17,55] which allows all ligand binding steps to be treated as a quasi-equilibrium governed by a single binding constant

$$K_{d,i} = \frac{[C_i]}{[C_iL]}[L] \tag{11}$$

where i labels the conformational state (unfolded U, antiparallel G4 A, or parallel/hybrid G4 P), C_i is the ligand-free conformation, C_iL is the ligand-bound conformation, L is the ligand (in this case, Na^+), and the square brackets indicate concentration of the enclosed species. The fraction of ligand-bound molecules is therefore

$$\theta_{bound,i} = \frac{[C_iL]}{[C_i] + [C_iL]} = \frac{[L]}{[L] + K_{d,i}} \tag{12}$$

Transitions between conformations are governed by first-order rate constants, depending on ligand occupancy:

$$C_i \xrightarrow{k_{ij,apo}} C_j \tag{13}$$

$$C_iL \xrightarrow{k_{ij,holo}} C_jL \tag{14}$$

where $k_{ij,apo}$ and $k_{ij,holo}$ are rate constants for the transition from state i to state j in the ligand-free ("apo") and ligand-bound ("holo") forms, respectively. The observed rate constants $k_{ij,obs}$ for transitions between conformational states are population-weighted averages of the apo and holo rate constants:

$$k_{ij,obs} = k_{ij,apo}\left(\frac{K_{d,i}}{[L] + K_{d,i}}\right) + k_{ij,holo}\left(\frac{[L]}{[L] + K_{d,i}}\right) \tag{15}$$

For the six-state kinetic model in Figure 4D, eq 15 forms a system of six equations, where the number of free parameters in the model can be reduced to 11 by imposing detailed balance constraints ($\Delta G_{cycle} = 0$) on all cycles. The resulting constrained equations are then globally fit to the kinetic data in Figure 4B, as summarized by the solid line fits.

The results of the six-state fit indicate that Na^+ promotes G4 folding through a "bind-then-fold" mechanism: Na^+ binds to the unfolded (U) state, which subsequently folds into a G4 (A

https://doi.org/10.1021/acs.jpcb.3c01001
J. Phys. Chem. B 2023, 127, 6842−6855

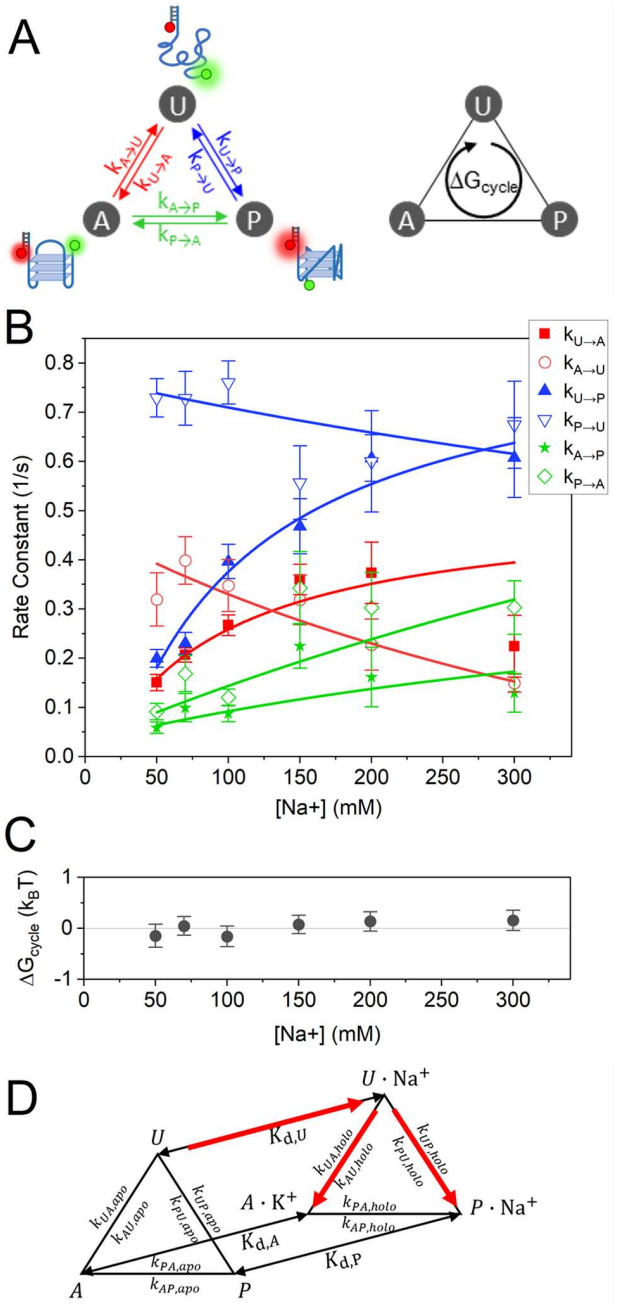

Figure 4. Influence of Na^+ on G4 folding kinetics. (A) Left: a structure of the hidden Markov model (HMM) that is used to fit the smFRET trajectories in order to obtain the G4 folding rate constants. Right: the orientation of the three-state cycle used to calculate the free energy change around the loop, $\Delta G_{cycle} = \Delta G_{U\to P} + \Delta G_{P\to A} + \Delta G_{A\to U}$. (B) The rate constants for G4 folding in 50−300 mM Na^+. Fits to the six-state Na^+ binding model that is depicted in (D) are shown as solid curves. (C) A plot of ΔG_{cycle} at each $[Na^+]$. To satisfy detailed balance conditions, ΔG_{cycle} must equal zero. (D) A six-state "Toblerone" connectivity model for the influence of Na^+ on G4 folding kinetics. The dominant pathways through this network are shown as red arrows, which reflect a "bind-then-fold" mechanism.

or P) topology (Figure 4D, pathways highlighted in red).[56−58] There are several key indicators in support of this mechanism. First, the forward folding rate constants $k_{U\to A}$ and $k_{U\to P}$ both vanish at low $[Na^+]$ (Figure 4B, filled red and blue symbols, respectively), which implies that folding to either of the G4 topologies without Na^+ is, evidently, impossible ($k_{UA,apo} = k_{UP,apo} = 0\ s^{-1}$). Additionally, $k_{U\to A}$ and $k_{U\to P}$ saturate at high $[Na^+]$ ($k_{UA,holo} = 0.7 \pm 0.3\ s^{-1}$, $k_{UP,holo} = 1.0 \pm 0.4\ s^{-1}$), which indicates that binding of Na^+ to the G4 is driven to completion. However, there is also a weaker dependence of the unfolding rate constants $k_{A\to U}$ and $k_{P\to U}$ on $[Na^+]$, so other pathways besides the induced fit ("bind-then-fold") pathway must be permitted to a lesser degree.

K^+ Has a Much Higher Affinity Than Na^+ for the G-Quadruplex and Exclusively Promotes the Parallel/Hybrid Topology. Formation of G-quadruplexes is known to be more sensitive to K^+ than to Na^+, which we next explore in order to measure the specific effects K^+ versus Na^+ has on G4 folding (Figure 5). Interestingly, K^+ drives the conformational equilibrium of the G4 smFRET construct exclusively toward the parallel/hybrid G4 (P) topology (Figure 5A), in essence, by depleting both the unfolded (U) and antiparallel G4 (A) states. Furthermore, this dramatic increase in folding occurs at only a few millimolar K^+ concentrations, in contrast to the 100-fold higher concentrations of Na^+ that is required to achieve folding (Figure 3B). Thus, the G4 construct clearly has a much higher affinity for K^+ than Na^+, though only in achieving the parallel/hybrid G4 conformation. Fitting the full suite of the K^+-dependent population data (Figure 5B) to a three-state Hill model quantitatively confirms these qualitative observations, as summarized in Table 1. In this case, there is no K^+ uptake during the transition from the unfolded state to the antiparallel G4 ($\Delta n_{U\to A} = -0.05 \pm 0.05$), which indicates that K^+ does not participate in this process. Meanwhile, approximately one cation binds during folding into the parallel/hybrid G4 ($\Delta n_{U\to P} = 0.62 \pm 0.05$), with a K^+ binding affinity ($K_d(K^+) = 1.9 \pm 0.2$ mM) that is two orders of magnitude greater than that of Na^+ ($K_d(Na^+) = 228 \pm 26$ mM) to achieve the same conformational state. The Hill coefficient being less than unity indicates that the parallel/hybrid G4 forms to a limited degree in the absence of the K^+ cation, which is consistent with the observed formation of the parallel/hybrid G4 in an Na^+-only buffer (Figure 3). We note that the K^+ binding affinity reported here is in good agreement with previous bulk studies by Largy et al. ($K_d(K^+) = 1-5$ mM), which were also performed in Na^+-rich solutions.[28] This agreement between fluorophore-labeled G4s and fluorophore-free G4s is evidence that the presence of the Cy3 and Cy5 fluorophores does not significantly perturb the G4 folding equilibrium, or at least cation binding to the G4, despite the fact that cyanine-based dyes are known to readily stack on G-tetrads.[59] By driving the G4 construct exclusively to the parallel/hybrid topology, K^+ thereby exerts a much greater restriction over G4 polymorphism than Na^+.

Similar to the analysis of the Na^+-dependent G4 folding kinetics described above, smFRET trajectories are subjected to hidden Markov modeling in order to extract rate constants as a function of $[K^+]$ (Figure 5C). As before, we can rigorously confirm these kinetic results by verifying that the rate constants explicitly obey a detailed balance ($\Delta G_{cycle} = 0$) at all K^+ concentrations (Figure 5D). Five of the six folding rate constants show little to no dependence on the K^+ concentration, while the rate constant for unfolding from the parallel/hybrid G4 to the unfolded state ($k_{P\to U}$) is strongly suppressed by the presence of K^+. To explore the mechanistic implications of these data, the folding rate constants are fit to the six-state kinetic model (eq 15) and overlaid on Figure 5C as solid lines. The fit correctly predicts that $k_{P\to U}$ goes to zero in the high $[K^+]$ limit ($k_{PT,holo} = 0.01 \pm 0.03\ s^{-1}$), which is

https://doi.org/10.1021/acs.jpcb.3c01001
J. Phys. Chem. B 2023, 127, 6842−6855

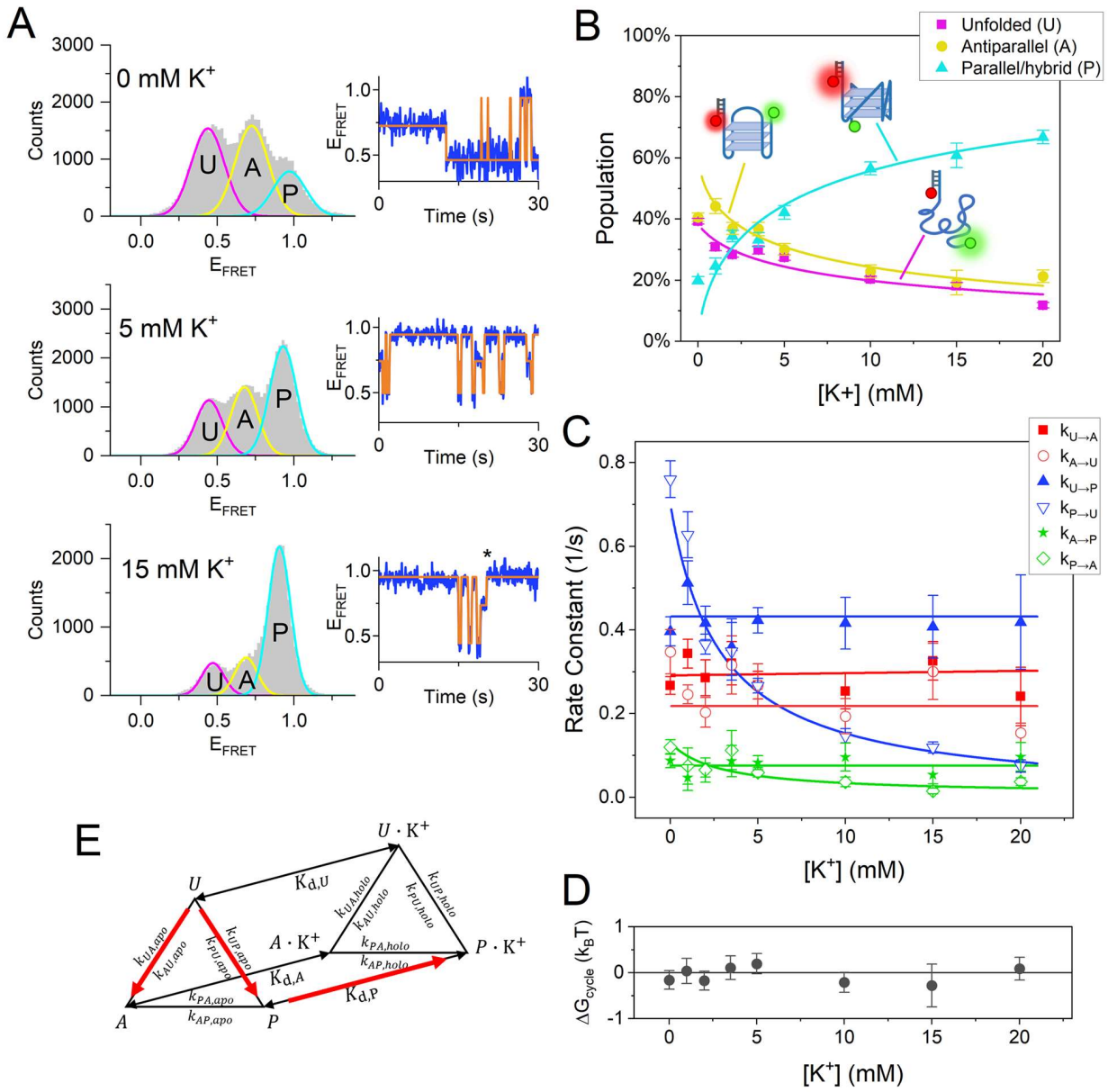

Figure 5. Influence of K^+ on G4 folding. (A) FRET histograms and sample FRET trajectories in 100 mM Na^+ with 0, 5, and 15 mM K^+. An example of a direct A → P transition is indicated by an asterisk. (B) State populations and (C) folding rate constants determined in 100 mM Na^+ with 0−20 mM K^+. Data are fit to a three-state Hill model in (B) and a six-state ligand binding model in (C). (D) The calculation of ΔG_{cycle} at each K^+ concentration to confirm that the rate constants satisfy detailed balance conditions. (E) A six-state model of K^+ binding to G4. Red arrows indicate the highest flux pathways (a "fold-then-bind" mechanism).

consistent with a conformational selection (CS, "fold-then-bind") model in which the apo DNA prefolds to a transient parallel/hybrid G4 state before binding to K^+ with high affinity ($K_{d,A}$ = 2.6 ± 1.2 mM) in order to stabilize the parallel/hybrid configuration. The K^+-induced folding pathways (red, highlighted in Figure 5E) contrast strongly with those predicted from the induced fit (IF, "bind-then-fold") mechanism seen in the Na^+-stabilized formation (see Figure 4D) of the G4 quadruplex and originate from a much stronger and topology-specific binding interaction.

Temperature Dependence of G-Quadruplex Folding Equilibria and Kinetics. Temperature-controlled single-molecule experiments can be used to deconstruct the overall free energy of G-quadruplex folding into enthalpic and entropic contributions.[49] The temperature dependence of the folding rate constants and equilibrium constants in 100 mM Na^+ is captured in Figure 6 over a temperature range of 13−29 °C. The rate constant (*y*-axis) scale in Figure 6 is logarithmic, which highlights the exponential dependence of the rate constants on temperature. To the best of our knowledge, this is the first time smFRET has been used to examine temperature-dependent kinetics for a nonbinary system with multiple (≥3) conformations. First, we observe from the *y*-axis scale that the majority of the conformational transitions involve the unfolded (U) state (Figure 6A,B, left panels), with direct folding and unfolding between the antiparallel G4 (A) and parallel/hybrid G4 (P) being minor kinetic processes at all temperatures (Figure 6C, left). Second, we observe the equilibrium

https://doi.org/10.1021/acs.jpcb.3c01001
J. Phys. Chem. B 2023, 127, 6842−6855

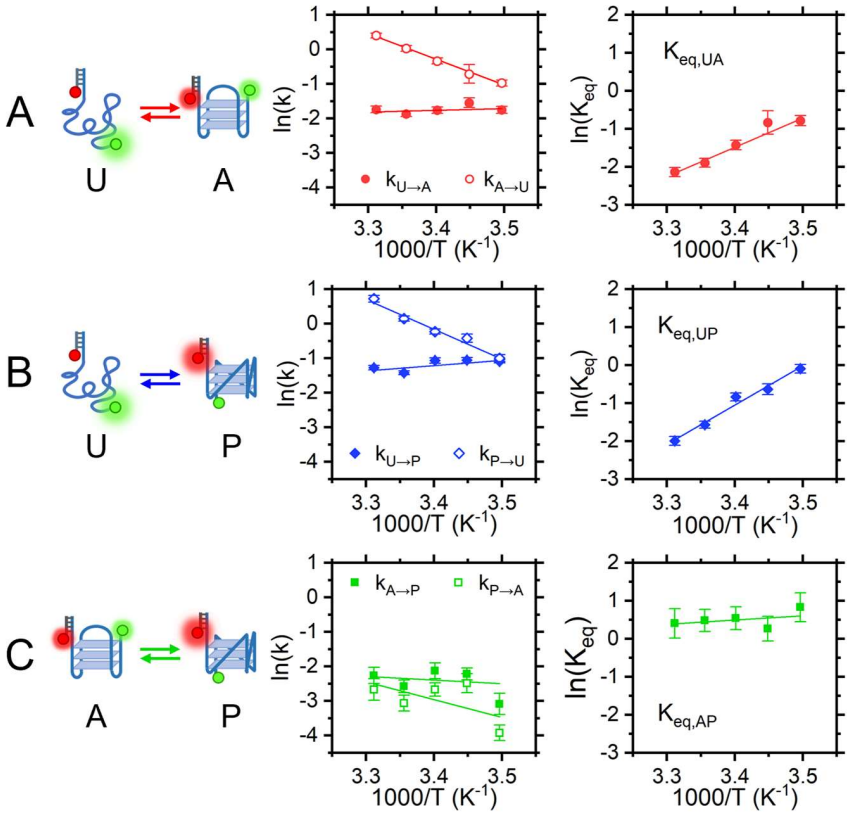

Figure 6. The temperature dependence of G4 folding rate constants (left panels) and equilibrium constants (right panels) in 100 mM Na^+ for (A) unfolded → antiparallel G4, (B) unfolded → parallel/hybrid G4, and (C) antiparallel G4 → parallel/hybrid G4 transitions. The solid lines indicate Arrhenius and van't Hoff fits for the rate constants and equilibrium constants, respectively, which are used to extract the enthalpy and entropy change for each process.

constants for folding from the U state to both G4 states ($K_{eq,UA}$ and $K_{eq,UP}$) decrease at high temperature, which demonstrates that the overall folding process is enthalpically favorable. The kinetic origin of this behavior is confirmed by examining the corresponding rate constants: the forward rate constants ($k_{U\to A}$ and $k_{U\to P}$) are largely temperature insensitive, which indicates a negligible activation enthalpy, while the reverse rate constants ($k_{A\to U}$ and $k_{P\to U}$) strongly increase with temperature, which is indicative of an enthalpic barrier for unfolding.

A more quantitative analysis can be carried out by fitting the rate constants and equilibrium constants to Arrhenius and van't Hoff models, respectively, from which overall and activation enthalpies (ΔH°, $\Delta H^\ddagger$, from slopes) and entropies (ΔS°, $\Delta S^\ddagger$, from intercepts) are determined. The thermodynamic values obtained from such three-state fits can, in turn, be used to construct 3D folding energy landscapes (see Figure 7), which depict the enthalpy (ΔH), entropy ($-T\Delta S$), and free energy (ΔG) contributions for each of the G-quadruplex conformations and intervening transition states. The enthalpic landscape (Figure 7A) reveals that both folding processes (U → A (red) and U → P (blue)) are enthalpically favorable ($\Delta H^\circ_{UA} = -66 \pm 7$ kJ/mol, $\Delta H^\circ_{UP} = -84 \pm 9$ kJ/mol) with a negligible barrier ($\Delta H^\ddagger_{UA} = -4 \pm 6$ kJ/mol, $\Delta H^\ddagger_{UP} = -13 \pm 6$ kJ/mol). Meanwhile, the entropy landscape (Figure 7B) indicates that folding is entropically costly ($\Delta S^\circ_{UA} = -240 \pm 20$ J/mol K, $\Delta S^\circ_{UP} = -300 \pm 30$ J/mol K), with an entropic penalty of ≈50% being achieved upon reaching the transition state ($\Delta S^\ddagger_{UA} = -140 \pm 20$ J/mol K, $\Delta S^\ddagger_{UP} = -170 \pm 20$ J/mol K). The overall free energy changes for folding (Figure 7C) are relatively small in comparison to the individual contributions from the enthalpy (ΔH) and entropy ($-T\Delta S$). Indeed, as an example of enthalpy−entropy compensation, these two contributions cancel nearly quantitatively to yield small overall free energy changes while still maintaining large free energy transition state barriers.[60,61]

Thermodynamics of G-Quadruplex Folding at Elevated Monovalent Cation Concentrations. To probe the effects of Na^+ and K^+ cations on folding thermodynamics, we have repeated these temperature-dependent studies of the G-quadruplex under multiple cation conditions. The temperature dependence for G-quadruplex folding under ambient (100 mM) Na^+, high (200 mM) Na^+, and 100 mM Na^+ with 4 mM K^+ are shown in Figure 8, where the latter two data sets can be compared to the first in order to isolate the impact due to Na^+ versus that due to K^+, respectively. Arrhenius and van't Hoff analyses are performed on each of the data sets, with the fitted entropic and enthalpic parameters for the three cationic conditions (100 mM Na^+, 200 mM Na^+, and 100 mM Na^+ with 4 mM K^+) shown side by side in Table 2.

The dependence of the folding enthalpies and entropies on cation concentration can be used to determine the thermodynamic "signature" (i.e., the sign of $\Delta\Delta H^\circ$ and $\Delta\Delta S^\circ$) of Na^+ and K^+ binding. For example, we first consider the change in the folding enthalpy of the unfolded to the parallel/hybrid G4 transition upon an increase in [Na^+] from 100 to 200 mM, defined as

$$\Delta\Delta H^\circ_{UP}(Na^+) \equiv \Delta H^\circ_{UP}(200\ \text{mM}\ Na^+) - \Delta H^\circ_{UP}(100\ \text{mM}\ Na^+) \quad (16)$$

https://doi.org/10.1021/acs.jpcb.3c01001
J. Phys. Chem. B 2023, 127, 6842−6855

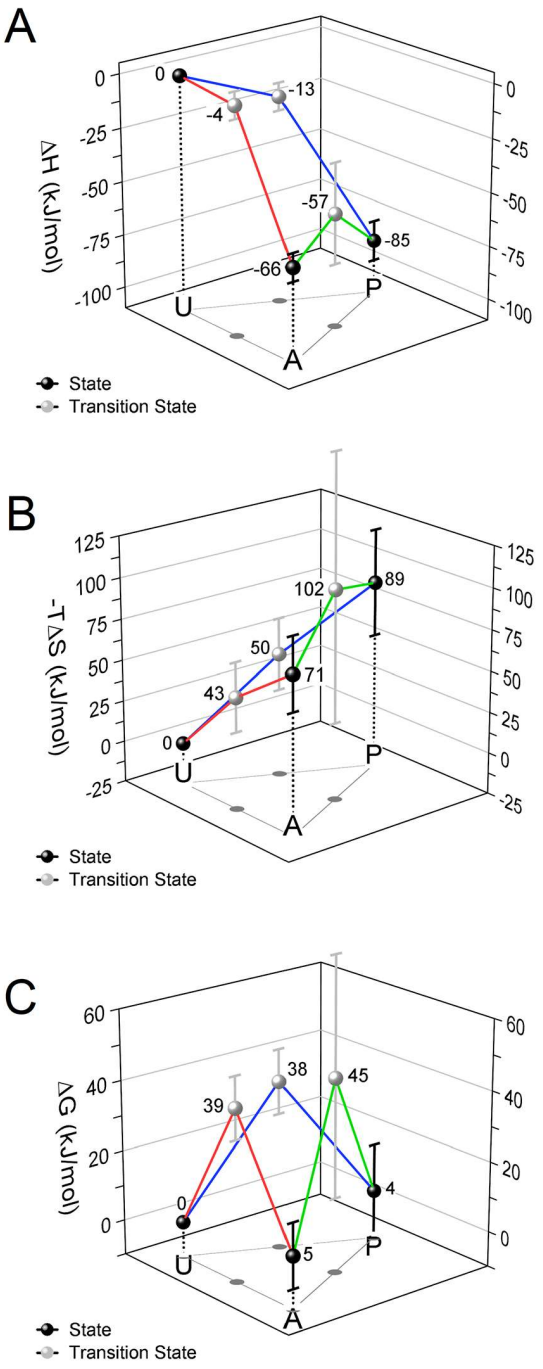

Figure 7. Folding landscape for G4 in 100 mM Na^+, as determined by van't Hoff and Arrhenius analyses. (A) The enthalpy (ΔH) of each stable conformation (black points) and transition state (light gray points), defined relative to the unfolded state, U. (B) The same as (A), but for the enthalpic contribution to the free energy ($-T\Delta S$) evaluated at 300 K. (C) The same as (A), but for the free energy ($\Delta G = \Delta H - T\Delta S$) evaluated at 300 K.

The results in Table 2 show that this quantity is positive ($\Delta\Delta H^\circ_{UP}(Na^+) = 40 \pm 11$ kJ/mol). Because Na^+ interacts with the G4 construct through a "bind-then-fold" mechanism, $\Delta\Delta H^\circ_{UP}(Na^+)$ is opposite in sign to the enthalpy of Na^+ binding, $\Delta H^\circ_{bind,Na}$, as depicted in Figure 9A. Therefore, since $\Delta\Delta H^\circ_{UP}(Na^+) > 0$, we can infer that Na^+ binding is enthalpically favorable ($\Delta H^\circ_{bind,Na} < 0$). We also observe that the Na^+-induced change in the folding entropy for this process is positive ($\Delta\Delta S^\circ_{UP}(Na^+) = 140 \pm 40$ J/mol K). Thus, by a similar logic, Na^+ binding must result in a loss of entropy ($\Delta S^\circ_{bind,Na} < 0$). Together, $\Delta H^\circ_{bind,Na}$ and $\Delta S^\circ_{bind,Na}$ indicate that Na^+ binding is consistent with the formation of energetically stable contacts with the unfolded G4 at the entropic cost of restricting the translational freedom of Na^+ and/or the conformational flexibility of the unfolded DNA.

Similarly, the thermodynamics of K^+ binding to the parallel/hybrid G4 can be determined by examining the differential folding enthalpy ($\Delta\Delta H^\circ_{UP}(K^+)$) and entropy ($\Delta\Delta S^\circ_{UP}(K^+)$) upon the addition of K^+, in this case defined as

$$\Delta\Delta H^\circ_{UP}(K^+) \equiv \Delta H^\circ_{UP}(100\ \text{mM}\ Na^+, 4\ \text{mM}\ K^+) - \Delta H^\circ_{UP}(100\ \text{mM}\ Na^+) \quad (17)$$

and

$$\Delta\Delta S^\circ_{UP}(K^+) \equiv \Delta S^\circ_{UP}(100\ \text{mM}\ Na^+, 4\ \text{mM}\ K^+) - \Delta S^\circ_{UP}(100\ \text{mM}\ Na^+) \quad (18)$$

In contrast to interactions mediated by Na^+, K^+ interacts with the G-quadruplex through a "fold-then-bind" mechanism and, as a result, $\Delta\Delta H^\circ_{UP}(K^+)$ and $\Delta\Delta S^\circ_{UP}(K^+)$ have the same sign as $\Delta H^\circ_{bind,K}$ and $\Delta S^\circ_{bind,K}$, respectively (Figure 9B). The observed $\Delta\Delta H^\circ_{UP}(K^+)$ and $\Delta\Delta S^\circ_{UP}(K^+)$ are both positive, which indicates that K^+ binding is enthalpically unfavorable ($\Delta H^\circ_{bind,K} > 0$) and entropically favorable ($\Delta S^\circ_{bind,K} > 0$). Interestingly, the signs of these thermodynamic parameters are exactly opposite to those of Na^+ binding, a fact that serves to emphasize the disparate natures of Na^+ and K^+ binding to the G-quadruplex construct.

IV. DISCUSSION

In this work, we have used the 5′-GGG-$(TAAGGG)_3$-3′ DNA G-quadruplex (TAA-G4) as a model system for understanding the thermodynamic influence of monovalent cations Na^+ and K^+ on G-quadruplex folding. The TAA-G4 sequence is similar to the human telomere G-quadruplex repeat (5′-TTAGGG-3′), with enhanced polymorphism due to the T → A mutation in the loop sequence.[34] The TAA-G4 is incorporated into a DNA construct designed for single-molecule FRET (smFRET) microscopy. The observed smFRET data reveal that the TAA-G4 populates three interconverting FRET states (Figure 2), a finding that is in agreement with previous single-molecule measurements made by Tippana et al. on a similar TAA-G4 construct.[34] From the smFRET trajectories, equilibrium constants and rate constants for transitions among the three states can be measured, with the dependence of these kinetic quantities obtained as a function of cation concentration and temperature.

We assigned structures to the three FRET states (low, middle, and high) as an unfolded state (U), an antiparallel G4 state (A), and a parallel or hybrid G4 state (P), respectively. Unfortunately, we are unable to further dissect the observed G4 folds by smFRET alone, such as distinguishing between chair versus basket antiparallel states or between parallel versus 3 + 1 hybrid versus 1 + 3 hybrid states. We note that the order of the A and P FRET efficiencies ($E_{antiparallel} < E_{parallel}$) is the reverse of that observed by Tippana et al. for the same G4 sequence.[34] However, the Tippana et al. smFRET construct incorporated the G4 fold that is directly adjacent to duplex DNA, whereas the G4 in our construct is connected to single-

https://doi.org/10.1021/acs.jpcb.3c01001
J. Phys. Chem. B 2023, 127, 6842−6855

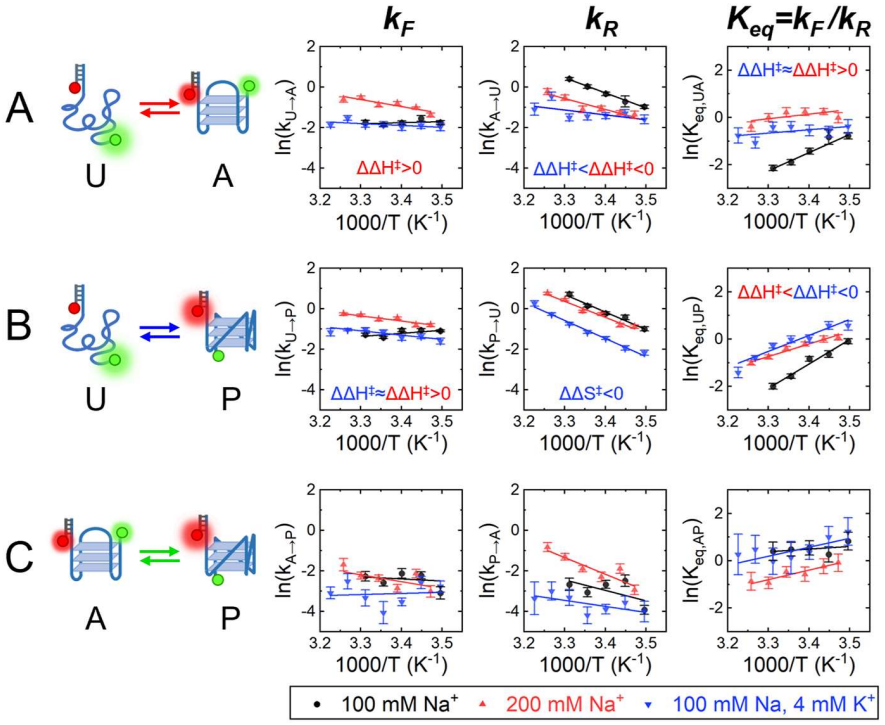

Figure 8. Temperature response of G4 folding under multiple cationic conditions (100 mM Na^+ in black, 200 mM Na^+ in red, and 100 mM Na^+ with 4 mM K^+ in blue) for the three G4 dynamic processes: (A) unfolded → antiparallel G4, (B) unfolded → parallel/hybrid G4, and (C) antiparallel G4 → parallel/hybrid G4. Arrhenius plots for the forward and reverse rate constants are shown in the left and middle panels, respectively, while van't Hoff plots for the equilibrium constants are shown in the right panels.

Table 2. Thermodynamic Parameters for G-Quadruplex Folding Determined by van't Hoff and Arrhenius Analyses of Temperature-Dependent Kinetic Measurements at Multiple Cation Concentrations (Figure 8)[a]

		100 mM Na^+	200 mM Na^+	100 mM Na^+, 4 mM K^+
		ΔH (kJ/mol)		
Unfolded → G4 (Antiparallel)	ΔH°_{TA}	−66 ± 7	−16 ± 9*	−12 ± 14*
	$\Delta H^\ddagger_{TA}$	−4 ± 6	29 ± 6*	8 ± 6
	$\Delta H^\ddagger_{AT}$	62 ± 2	45 ± 7*	20 ± 13*
Unfolded → G4 (Parallel/Hybrid)	ΔH°_{TP}	−85 ± 9	−44 ± 7*	−56 ± 6*
	$\Delta H^\ddagger_{TP}$	−13 ± 6	21 ± 4*	18 ± 4*
	$\Delta H^\ddagger_{PT}$	72 ± 7	66 ± 6	74 ± 4
G4 (Antiparallel) → G4 (Parallel/Hybrid)	ΔH°_{AP}	−34 ± 40	−40 ± 25	−29 ± 24
	$\Delta H^\ddagger_{AP}$	9 ± 23	28 ± 19	−5 ± 18
	$\Delta H^\ddagger_{PA}$	43 ± 33	68 ± 15	25 ± 16
		ΔS(J/mol K)		
Unfolded → G4 (Antiparallel)	ΔS°_{TA}	−240 ± 20	−50 ± 30*	−50 ± 50*
	$\Delta S^\ddagger_{TA}$	−140 ± 20	−30 ± 20*	−100 ± 20
	$\Delta S^\ddagger_{AT}$	90 ± 10	30 ± 20*	−60 ± 40*
Unfolded → G4 (Parallel/Hybrid)	ΔS°_{TP}	−300 ± 30	−150 ± 20*	−190 ± 20*
	$\Delta S^\ddagger_{TP}$	−170 ± 20	−50 ± 10*	−70 ± 10*
	$\Delta S^\ddagger_{PT}$	130 ± 20	100 ± 20	120 ± 10
G4 (Antiparallel) → G4 (Parallel/Hybrid)	ΔS°_{AP}	−110 ± 140	−140 ± 80	−90 ± 80
	$\Delta S^\ddagger_{AP}$	−100 ± 80	−40 ± 70	−160 ± 60
	$\Delta S^\ddagger_{PA}$	10 ± 110	100 ± 50	−60 ± 50

[a]Uncertainties are reported as standard errors of the mean. Asterisks indicate statistical significance (evaluated at the p = 0.01 level) of the parameters when compared to the 100 mM Na^+ case.

https://doi.org/10.1021/acs.jpcb.3c01001
J. Phys. Chem. B 2023, 127, 6842−6855

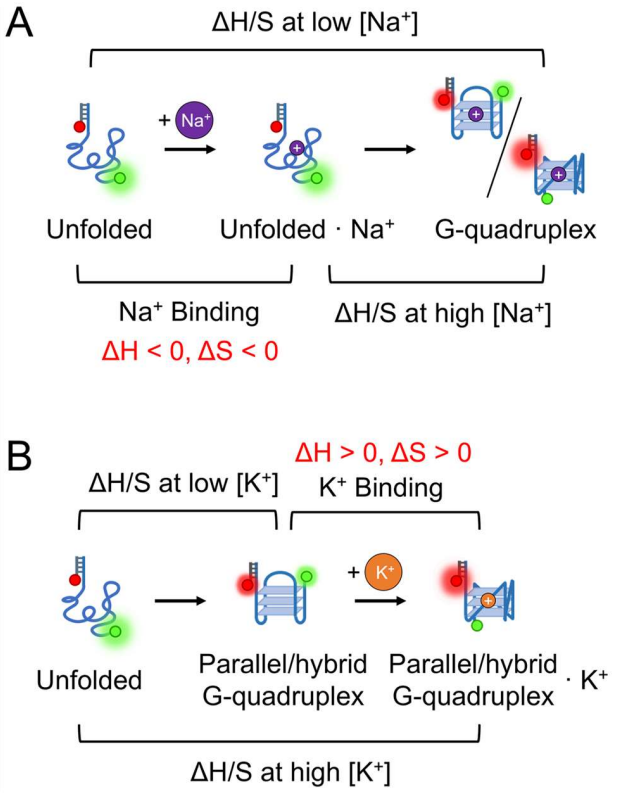

Figure 9. Determination of cation binding thermodynamics. (A) For Na^+, which follows a "bind-then-fold" model, the measured enthalpy/entropy ($\Delta H/S$) at low [Na^+] contains contributions from both Na^+ binding ($\Delta H/S_{bind}$) and the conformational change ($\Delta H/S_{conf}$). However, at high [Na^+], the unfolded conformation saturates with Na^+, and $\Delta H/S$ reflects only $\Delta H/S_{conf}$. Therefore, $\Delta\Delta H/S = \Delta H/S$(high [$Na^+$]) − $\Delta H/S$(low [Na^+]) has the opposite sign of $\Delta H/S_{bind}$. (B) For K^+, which operates by a "fold-then-bind" mechanism, the differential enthalpy/entropy $\Delta\Delta H/S = \Delta H/S$(high [$K^+$]) − $\Delta H/S$(low [K^+]) has the same sign as $\Delta H/S_{bind}$.

stranded DNA. Indeed, our observed FRET orderings agree with that of Ray et al., who examined G4s flanked by single-stranded DNA.[62] Clearly, the folding geometry of G-quadruplexes, and thus the ordering of the FRET states, can be quite sensitive to the local sequence environment.

Monovalent cations drive the TAA-G4 folding equilibrium from the unfolded state into the antiparallel and parallel/hybrid G4 states in a cation-specific fashion. K^+ exclusively promotes the parallel/hybrid configuration (Figure 5A,B), while Na^+ permits both configurations with a small preference for the antiparallel topology (Figure 3). Furthermore, concentration-dependent kinetics (Figures 4C and 5C) reveal that Na^+ and K^+ promote G-quadruplex folding through distinctly different kinetic mechanisms. For Na^+, the cation binds to the unfolded state before the ligand-bound complex folds into one of the G-quadruplex configurations (Figure 4D, a "bind-then-fold" mechanism). In contrast, the TAA-G4 sequence must first fold into the parallel/hybrid G4 topology before K^+ will bind to form a stabilized complex (Figure 5E, a "fold-then-bind" mechanism). The fact that these two monovalent cations act on the TAA-G4 via such different mechanisms reinforces how responsive G-quadruplexes are to their environment or, in this case, cation size. We present a simplified, combined kinetic model of Na^+- and K^+-induced folding of G-quadruplexes in Figure 10. In this model, Na^+ binding is a prerequisite for unfolded to quadruplex transitions,

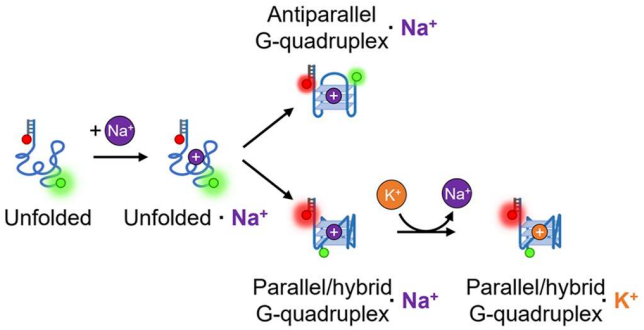

Figure 10. Proposed scheme of Na^+ and K^+ binding to TAA-G4.

after which the parallel/hybrid configuration of the G4 can subsequently bind to a K^+ ion, perhaps by replacing Na^+ (as shown in the figure) or by attaching to an alternative binding site. It is possible and even likely that the identified Na^+ binding site has a similar affinity for other monovalent cations including K^+, but the much higher affinity of the K^+-specific binding site means that our K^+ titrations saturate before lower affinity binding to the triplex can be observed.

Titrations of K^+ and Na^+ indicate that the G4 construct binds to a single cation during folding (Figures 3 and 5). This observation is surprising in light of G4 crystal structures, which routinely indicate that G4s with three tetrads, as studied here, bind to two monovalent cations.[16] One explanation for this disagreement is that the low FRET state is not fully unfolded, but rather a partially folded G4 intermediate that is already bound to one cation. If that is the case, the cation binding observed in this work is, in fact, the recruitment of the second cation that is required for G4 folding. Promising G4 intermediates to fill this role include a G-duplex, a G-triplex, or a two-tetrad structure, each of which has been previously shown to bind to a single cation.[14,28] However, the existence of such structures as metastable G4 intermediates is disputed,[63] and more work is required to elucidate this issue. Nevertheless, the observed cation binding stoichiometry in this work provides further evidence of a folding intermediate with a single bound cation, though such a structure must be noncompact in order to have a FRET efficiency that is indistinguishable from a fully unfolded structure (Figure 2D).

To explore the influence of Na^+ and K^+ on the thermodynamics of TAA-G4 folding, temperature-dependent experiments have been pursued to obtain the folding enthalpies and entropies as a function of cation concentration. By considering the changes in the thermodynamic variables upon an increase in [Na^+] or [K^+], we can infer the thermodynamic impact of cation binding. Interestingly, the folding thermodynamics (ΔH° and ΔS°) of the TAA-G4 construct respond similarly to the addition of either 100 mM Na^+ or 4 mM K^+, as summarized in Table 2. However, because Na^+ and K^+ interact with the TAA-G4 through different mechanisms ("bind-then-fold" versus "fold-then-bind"), we can conclude that the signs of the enthalpy and entropy changes for Na^+ binding are opposite to those of K^+ binding (Figure 9). Specifically, Na^+ binding to the U conformation is driven by enthalpically favorable interactions ($\Delta H^\circ_{bind,Na} < 0$) that outweigh a loss of entropy ($\Delta S^\circ_{bind,Na} < 0$), perhaps due to a conformational restriction upon ion binding. In contrast, K^+

https://doi.org/10.1021/acs.jpcb.3c01001
J. Phys. Chem. B 2023, 127, 6842−6855

binds to the parallel/hybrid G4 topology in an entropically driven process ($\Delta S^{\circ}_{bind,K} > 0$) that occurs at an enthalpic cost ($\Delta H^{\circ}_{bind,K} > 0$). One explanation of this entropically driven binding is that K^+ replaces a loosely fitting Na^+ in the binding pocket in order to form a more compact G-quadruplex, resulting in the expulsion of surface-bound water molecules. Such a release of water molecules would be entropically favorable, yet energetically costly, due to the breaking of hydrogen bonds between the water molecules and the nucleic acid. This hypothesis of G-quadruplex compaction and water release upon K^+ binding is generally supported in the literature with studies of the ion-dependent folding volumes for the G-quadruplex,[64,65] though one study reports that K^+ produces larger G4 volumes than Na^+.[23] Clearly, further study is needed to elucidate this feature of G4 folding, such as with pressure-dependent single-molecule folding experiments.[66]

V. CONCLUSIONS

In this work, we explored the influence of monovalent cations on G-quadruplex folding through single-molecule temperature-controlled kinetic measurements. With the novel use of smFRET to measure the temperature-dependent folding kinetics on a system with more than two FRET conformations, we observe three-state G-quadruplex folding ascribed to conformational transitions between an unfolded state and two G-quadruplex topologies. Concentration-dependent measurements show that the Na^+ binds to the unfolded state and remains bound while G-quadruplex topologies are sampled. In contrast, K^+ binds exclusively to the parallel/hybrid G-quadruplex conformation and has a binding affinity approximately 100 times larger than that of Na^+. The thermodynamics of Na^+ binding are enthalpically driven ($\Delta H^{\circ}_{bind,Na} < 0$, $\Delta S^{\circ}_{bind,Na} < 0$), while the thermodynamics of K^+ binding are entropically driven ($\Delta H^{\circ}_{bind,K} > 0$, $\Delta S^{\circ}_{bind,K} > 0$), likely due to G4 compaction and concomitant water release.

AUTHOR INFORMATION

Corresponding Author

David J. Nesbitt − *JILA, National Institute of Standards and Technology and University of Colorado, Boulder, Colorado 80309, United States; Department of Chemistry and Department of Physics, University of Colorado, Boulder, Colorado 80309, United States;* orcid.org/0000-0001-5365-1120; Email: djn@jila.colorado.edu

Author

David A. Nicholson − *JILA, National Institute of Standards and Technology and University of Colorado, Boulder, Colorado 80309, United States; Department of Chemistry, University of Colorado, Boulder, Colorado 80309, United States*

Complete contact information is available at: https://pubs.acs.org/10.1021/acs.jpcb.3c01001

Notes

The authors declare no competing financial interest.

ACKNOWLEDGMENTS

Initial support for this work was through the National Science Foundation under Grant CHE 2053117 from the Chemical, Structure, Dynamics, and Mechanisms-A Program, with recent transition to support from the Air Force Office of Scientific Research (FA9550-15-1-0090) and with additional funds for development of the TIRF apparatus from PHY-1734006 (Physics Frontier Center Program). We would also like to gratefully acknowledge predoctoral fellowship support from the National Institutes of Health Molecular Biophysics Training, Grant T32 GM-065103, as well as early seed contributions by the W. M. Keck Foundation Initiative in RNA Sciences at the University of Colorado, Boulder.

REFERENCES

(1) Dolinnaya, N. G.; Ogloblina, A. M.; Yakubovskaya, M. G. Structure, properties, and biological relevance of the DNA and RNA G-quadruplexes: Overview 50 years after their discovery. *Biochemistry (Moscow)* **2016**, *81*, 1602−1649.

(2) Rhodes, D.; Lipps, H. J. G-quadruplexes and their regulatory roles in biology. *Nucleic Acids Res.* **2015**, *43*, 8627−8637.

(3) Varshney, D.; Spiegel, J.; Zyner, K.; Tannahill, D.; Balasubramanian, S. The regulation and functions of DNA and RNA G-quadruplexes. *Nat. Rev. Mol. Cell Biol.* **2020**, *21*, 459−474.

(4) Zhao, C.; Qin, G.; Niu, J.; Wang, Z.; Wang, C.; Ren, J.; Qu, X. Targeting RNA G-quadruplex in SARS-CoV-2: A promising therapeutic target for COVID-19? *Angew. Chem., Int. Ed.* **2021**, *60*, 432−438.

(5) Neidle, S. Quadruplex nucleic acids as novel therapeutic targets. *J. Med. Chem.* **2016**, *59*, 5987−6011.

(6) Banerjee, N.; Panda, S.; Chatterjee, S. Frontiers in G-Quadruplex therapeutics in cancer: Selection of small molecules, peptides and aptamers. *Chem. Biol. Drug Des.* **2022**, *99*, 1−31.

(7) Yatsunyk, L. A.; Mendoza, O.; Mergny, J.-L. Nano-oddities": Unusual nucleic acid assemblies for DNA-based nanostructures and nanodevices. *Acc. Chem. Res.* **2014**, *47*, 1836−1844.

(8) Rajendran, A.; Endo, M.; Hidaka, K.; Lan Thao Tran, P.; Mergny, J.-L.; Sugiyama, H. Controlling the stoichiometry and strand polarity of a tetramolecular G-quadruplex structure by using a DNA origami frame. *Nucleic Acids Res.* **2013**, *41*, 8738−8747.

(9) Harkness, R. W.; Mittermaier, A. K. G-quadruplex dynamics. *Biochim. Biophys. Acta, Proteins Proteomics* **2017**, *1865*, 1544−1554.

(10) Burge, S.; Parkinson, G. N.; Hazel, P.; Todd, A. K.; Neidle, S. Quadruplex DNA: sequence, topology and structure. *Nucleic Acids Res.* **2006**, *34*, 5402−5415.

(11) Ma, Y.; Iida, K.; Nagasawa, K. Topologies of G-quadruplex: Biological functions and regulation by ligands. *Biochem. Biophys. Res. Commun.* **2020**, *531*, 3−17.

(12) Grün, J. T.; Schwalbe, H. Folding dynamics of polymorphic G-quadruplex structures. *Biopolymers* **2022**, *113*, No. e23477.

(13) Nguyen, T. Q. N.; Lim, K. W.; Phan, A. T. Folding kinetics of G-quadruplexes: Duplex stem loops drive and accelerate G-quadruplex folding. *J. Phys. Chem. B* **2020**, *124*, 5122−5130.

(14) Cerofolini, L.; Amato, J.; Giachetti, A.; Limongelli, V.; Novellino, E.; Parrinello, M.; Fragai, M.; Randazzo, A.; Luchinat, C. G-triplex structure and formation propensity. *Nucleic Acids Res.* **2014**, *42*, 13393−404.

(15) Hou, X.-M.; Fu, Y.-B.; Wu, W.-Q.; Wang, L.; Teng, F.-Y.; Xie, P.; Wang, P.-Y.; Xi, X.-G. Involvement of G-triplex and G-hairpin in the multi-pathway folding of human telomeric G-quadruplex. *Nucleic Acids Res.* **2017**, *45*, 11401−11412.

(16) Bhattacharyya, D.; Mirihana Arachchilage, G.; Basu, S. Metal cations in G-quadruplex folding and stability. *Front. Chem.* **2016**, *4*, 38.

(17) Largy, E.; Mergny, J.-L.; Gabelica, V. Role of alkali metal ions in G-quadruplex nucleic acid structure and stability. In *The Alkali Metal Ions: Their Role for Life*; Sigel, A., Sigel, H., Sigel, R. K. O., Eds.; Springer International Publishing, Cham, 2016, p 203−258.

(18) Nishio, M.; Tsukakoshi, K.; Ikebukuro, K. G-quadruplex: Flexible conformational changes by cations, pH, crowding and its applications to biosensing. *Biosens. Bioelectron.* **2021**, *178*, 113030.

(19) Parkinson, G. N.; Lee, M. P. H.; Neidle, S. Crystal structure of parallel quadruplexes from human telomeric DNA. *Nature* **2002**, *417*, 876−880.
(20) Luu, K. N.; Phan, A. T.; Kuryavyi, V.; Lacroix, L.; Patel, D. J. Structure of the human telomere in K+ solution: An intramolecular (3 + 1) G-quadruplex scaffold. *J. Am. Chem. Soc.* **2006**, *128*, 9963−9970.
(21) Lane, A. N.; Chaires, J. B.; Gray, R. D.; Trent, J. O. Stability and kinetics of G-quadruplex structures. *Nucleic Acids Res.* **2008**, *36*, 5482−5515.
(22) Chalikian, T. V.; Liu, L.; Macgregor, R. B. Jr. Duplex-tetraplex equilibria in guanine- and cytosine-rich DNA. *Biophys. Chem.* **2020**, *267*, 106473.
(23) Li, Y. Y.; Dubins, D. N.; Le, D. M. N. T.; Leung, K.; Macgregor, R. B. The role of loops and cation on the volume of unfolding of G-quadruplexes related to HTel. *Biophys. Chem.* **2017**, *231*, 55−63.
(24) Majhi, P. R.; Qi, J.; Tang, C.-F.; Shafer, R. H. Heat capacity changes associated with guanine quadruplex formation: An isothermal titration calorimetry study. *Biopolymers* **2008**, *89*, 302−309.
(25) Green, J. J.; Ying, L.; Klenerman, D.; Balasubramanian, S. Kinetics of unfolding the human telomeric DNA quadruplex using a PNA trap. *J. Am. Chem. Soc.* **2003**, *125*, 3763−7.
(26) Laouer, K.; Schmid, M.; Wien, F.; Changenet, P.; Hache, F. Folding dynamics of DNA G-quadruplexes probed by millisecond temperature jump circular dichroism. *J. Phys. Chem. B* **2021**, *125*, 8088−8098.
(27) Hatzakis, E.; Okamoto, K.; Yang, D. Thermodynamic stability and folding kinetics of the major G-quadruplex and its loop isomers formed in the nuclease hypersensitive element in the human c-Myc promoter: Effect of loops and flanking segments on the stability of parallel-stranded intramolecular G-quadruplexes. *Biochemistry* **2010**, *49*, 9152−9160.
(28) Largy, E.; Marchand, A.; Amrane, S.; Gabelica, V.; Mergny, J.-L. Quadruplex turncoats: Cation-dependent folding and stability of quadruplex-DNA double switches. *J. Am. Chem. Soc.* **2016**, *138*, 2780−2792.
(29) Sustarsic, M.; Kapanidis, A. N. Taking the ruler to the jungle: Single-molecule FRET for understanding biomolecular structure and dynamics in live cells. *Curr. Opin. Struct. Biol.* **2015**, *34*, 52−59.
(30) Maleki, P.; Budhathoki, J. B.; Roy, W. A.; Balci, H. A practical guide to studying G-quadruplex structures using single-molecule FRET. *Molecular genetics and genomics: MGG* **2017**, *292*, 483−498.
(31) Budhathoki, J. B.; Maleki, P.; Roy, W. A.; Janscak, P.; Yodh, J. G.; Balci, H. A comparative study of G-quadruplex unfolding and DNA reeling activities of human RECQ5 helicase. *Biophys. J.* **2016**, *110*, 2585−2596.
(32) Aznauryan, M.; Sondergaard, S.; Noer, S. L.; Schiott, B.; Birkedal, V. A direct view of the complex multi-pathway folding of telomeric G-quadruplexes. *Nucleic Acids Res.* **2016**, *44*, 11024−11032.
(33) Noer, S. L.; Preus, S.; Gudnason, D.; Aznauryan, M.; Mergny, J. L.; Birkedal, V. Folding dynamics and conformational heterogeneity of human telomeric G-quadruplex structures in Na+ solutions by single molecule FRET microscopy. *Nucleic Acids Res.* **2016**, *44*, 464−71.
(34) Tippana, R.; Xiao, W.; Myong, S. G-quadruplex conformation and dynamics are determined by loop length and sequence. *Nucleic Acids Res.* **2014**, *42*, 8106−8114.
(35) Jansson, L. I.; Hentschel, J.; Parks, J. W.; Chang, T. R.; Lu, C.; Baral, R.; Bagshaw, C. R.; Stone, M. D. Telomere DNA G-quadruplex folding within actively extending human telomerase. *Proc. Natl. Acad. Sci. U. S. A.* **2019**, *116*, 9350−9359.
(36) Arns, L.; Knop, J.-M.; Patra, S.; Anders, C.; Winter, R. Single-molecule insights into the temperature and pressure dependent conformational dynamics of nucleic acids in the presence of crowders and osmolytes. *Biophys. Chem.* **2019**, *251*, 106190.
(37) Lerner, E.; Cordes, T.; Ingargiola, A.; Alhadid, Y.; Chung, S.; Michalet, X.; Weiss, S. Toward dynamic structural biology: Two decades of single-molecule Forster resonance energy transfer. *Science* **2018**, *359*, 288.
(38) Smith, C. L.; Milea, J. S.; Nguyen, G. H. Immobilization of nucleic acids using biotin-strept(avidin) systems. In *Immobilisation of DNA on Chips II*; Wittmann, C., Ed.; Springer, Berlin, 2005, p 63−90.
(39) Nicholson, D. A.; Sengupta, A.; Sung, H.-L.; Nesbitt, D. J. Amino acid stabilization of nucleic acid secondary structure: Kinetic insights from single-molecule studies. *J. Phys. Chem. B* **2018**, *122*, 9869−9876.
(40) Nicholson, D. A.; Sengupta, A.; Nesbitt, D. J. Chirality-dependent amino acid modulation of RNA folding. *J. Phys. Chem. B* **2020**, *124*, 11561−11572.
(41) Aitken, C. E.; Marshall, R. A.; Puglisi, J. D. An oxygen scavenging system for improvement of dye stability in single-molecule fluorescence experiments. *Biophys. J.* **2008**, *94*, 1826−35.
(42) Ha, T.; Tinnefeld, P. Photophysics of fluorescent probes for single-molecule biophysics and super-resolution imaging. *Annu. Rev. Phys. Chem.* **2012**, *63*, 595−617.
(43) Axelrod, D. Total internal reflection fluorescence microscopy. In *Methods in Cell Biology*, 1st ed.; Elsevier Inc., 2008, Vol. *89*, p 169−221.
(44) Roy, R.; Hohng, S.; Ha, T. A practical guide to single-molecule FRET. *Nat. Methods* **2008**, *5*, 507−16.
(45) Chodera, J. D.; Noe, F. Markov state models of biomolecular conformational dynamics. *Curr. Opin. Struct. Biol.* **2014**, *25*, 135−144.
(46) Hanson, S. M.; Ekins, S.; Chodera, J. D. Modeling error in experimental assays using the bootstrap principle: Understanding discrepancies between assays using different dispensing technologies. *J. Comput. Aided Mol. Des* **2015**, *29*, 1073−1086.
(47) Leipply, D.; Draper, D. E. Dependence of RNA tertiary structural stability on Mg^{2+} concentration: Interpretation of the Hill equation and coefficient. *Biochemistry* **2010**, *49*, 1843−1853.
(48) Mikulecky, P. J.; Feig, A. L. Heat capacity changes associated with nucleic acid folding. *Biopolymers* **2006**, *82*, 38−58.
(49) Holmstrom, E. D.; Nesbitt, D. J. Biophysical insights from temperature-dependent single-molecule Forster resonance energy transfer. *Annu. Rev. Phys. Chem.* **2016**, *67*, 441−65.
(50) Hori, N.; Denesyuk, N. A.; Thirumalai, D. Frictional effects on RNA folding: Speed limit and Kramers turnover. *J. Phys. Chem. B* **2018**, *122*, 11279−11288.
(51) Truex, K.; Chung, H. S.; Louis, J. M.; Eaton, W. A. Testing Landscape Theory for Biomolecular Processes with Single Molecule Fluorescence Spectroscopy. *Phys. Rev. Lett.* **2015**, *115*, 018101.
(52) Dupuis, N. F.; Holmstrom, E. D.; Nesbitt, D. J. Tests of Kramers' Theory at the Single-Molecule Level: Evidence for Folding of an Isolated RNA Tertiary Interaction at the Viscous Speed Limit. *J. Phys. Chem. B* **2018**, *122*, 8796−8804.
(53) McKinney, S. A.; Joo, C.; Ha, T. Analysis of single-molecule FRET trajectories using hidden Markov modeling. *Biophys. J.* **2006**, *91*, 1941−51.
(54) Lee, T. H. Extracting kinetics information from single-molecule fluorescence resonance energy transfer data using hidden Markov models. *J. Phys. Chem. B* **2009**, *113*, 11535−42.
(55) Deng, H.; Braunlin, W. H. Kinetics of sodium ion binding to DNA quadruplexes. *J. Mol. Biol.* **1996**, *255*, 476−483.
(56) Leulliot, N.; Varani, G. Current topics in RNA-protein recognition: Control of specificity and biological function through induced fit and conformational capture. *Biochemistry* **2001**, *40*, 7947−7956.
(57) Boehr, D. D.; Nussinov, R.; Wright, P. E. The role of dynamic conformational ensembles in biomolecular recognition. *Nat. Chem. Biol.* **2009**, *5*, 789−796.
(58) Du, X.; Li, Y.; Xia, Y. L.; Ai, S. M.; Liang, J.; Sang, P.; Ji, X. L.; Liu, S. Q. Insights into protein-ligand interactions: Mechanisms, models, and methods. *Int. J. Mol. Sci.* **2016**, *17*, 144.
(59) Nanjunda, R.; Owens, E. A.; Mickelson, L.; Alyabyev, S.; Kilpatrick, N.; Wang, S.; Henary, M.; Wilson, W. D. Halogenated pentamethine cyanine dyes exhibiting high fidelity for G-quadruplex DNA. *Bioorg. Med. Chem.* **2012**, *20*, 7002−11.

https://doi.org/10.1021/acs.jpcb.3c01001
J. Phys. Chem. B 2023, 127, 6842−6855

(60) Dunitz, J. D. Win some, lose some: Enthalpy-entropy compensation in weak intermolecular interactions. *Chem. Biol.* **1995**, *2*, 709−712.
(61) Fox, J. M.; Zhao, M.; Fink, M. J.; Kang, K.; Whitesides, G. M. The molecular origin of enthalpy/entropy compensation in biomolecular recognition. *Annu. Rev. Biophys.* **2018**, *47*, 223−250.
(62) Ray, S.; Bandaria, J. N.; Qureshi, M. H.; Yildiz, A.; Balci, H. G-quadruplex formation in telomeres enhances POT1/TPP1 protection against RPA binding. *Proc. Natl. Acad. Sci. U. S. A.* **2014**, *111*, 2990−5.
(63) Šponer, J.; Islam, B.; Stadlbauer, P.; Haider, S. Chapter Seven - Molecular dynamics simulations of G-quadruplexes: The basic principles and their application to folding and ligand binding. In *Annual Reports in Medicinal Chemistry*; Neidle, S., Ed.; Academic Press, 2020, Vol. *54*, p 197−241.
(64) Hellman, L. M.; Rodgers, D. W.; Fried, M. G. Phenomenological partial-specific volumes for G-quadruplex DNAs. *Eur. Biophys. J.* **2010**, *39*, 389−396.
(65) Knop, J.-M.; Patra, S.; Harish, B.; Royer, C. A.; Winter, R. The deep sea osmolyte trimethylamine N-oxide and macromolecular crowders rescue the antiparallel conformation of the human telomeric G-quadruplex from urea and pressure stress. *Chem. Eur. J.* **2018**, *24*, 14346−14351.
(66) Sung, H. L.; Nesbitt, D. J. Single-molecule kinetic studies of DNA hybridization under extreme pressures. *Phys. Chem. Chem. Phys.* **2020**, *22*, 23491−23501.

https://doi.org/10.1021/acs.jpcb.3c01001
J. Phys. Chem. B 2023, 127, 6842−6855